On the Compatibility of Halide Bilayer Separators for All-Solid-State Batteries

Abhishek A. Panchal,[†,§] Tyler N.T. Pennebaker,[‡,‖] Elias Sebti,[‡,‖] Yan Li,[¶] Yuheng Li,[¶] Raphaële J. Clément,[*,‡,‖] and Pieremanuele Canepa[*,†,§]

†*Department of Electrical and Computer Engineering, Houston, Texas, 77204, United States*

‡*Materials Department, University of California, Santa Barbara, California 93106, United States*

¶*Department of Materials Science and Engineering, National University of Singapore, 9 Engineering Drive 1, 117575, Singapore*

§*Texas Center for Superconductivity, University of Houston, Houston, Texas, 77204, United States*

‖*Materials Research Laboratory, University of California, Santa Barbara, California 93106, United States*

E-mail: rclement@ucsb.edu; pcanepa@uh.edu

Abstract

Considering the lack of solid electrolytes that are electrochemically stable in contact with a high-voltage cathode and a low-voltage metallic anode, bilayer separators in all-solid-state batteries are gaining increasing attention. However, previous studies have shown that the chemical reactivity between the materials comprising the electrolyte bilayer is one of the contributing factors to the deterioration of battery performance during cycling. Here, we computationally screen the chemical compatibility

of an extensive range of materials forming a bilayer separator using first-principles calculations. Notably, several bilayer separators are found to be thermodynamically stable, amongst them, the stability of the Li_3PO_4/Li_3InCl_6 pairing is further verified experimentally using a combination of X-ray diffraction, solid-state nuclear magnetic resonance, and X-ray photoelectron spectroscopy.This study underscores the importance of understanding the chemical compatibility of bilayer separators when engineering high-energy density all-solid-state batteries.

A net reduction of greenhouse gas emissions can be achieved by increasing the use of renewable energy sources, such as solar, wind, hydrothermal, and hydroelectric. However, most of these sources can only supply power intermittently and require energy storage platforms, such as rechargeable batteries, to deliver energy based on demand. Lithium-ion batteries (LIBs) are widely used as energy storage platforms in millions of portable devices. Still, LIBs have several shortcomings preventing their increased acceptance in vehicular transportation and large infrastructure installations. For example, LIBs rely on flammable liquid organic electrolytes, which pose a safety risk.[1] The gradual increase in the energy density of commercial LIBs witnessed over the past few decades is expected to level out save for disruptive innovations in materials chemistry and device architectures.[1] One promising path towards safer LIBs is the development of all-solid-state batteries (ASSBs),[2–4] comprising non-flammable inorganic solid electrolytes (SEs). While maintaining Li-ion conductivities comparable to or better than liquid electrolytes, SEs act as physical separators; they are perceived to improve safety by compartmentalizing the high reactivity of the anode and cathode materials, preventing any leakage and reducing gassing, which is common in liquid batteries.[3] In addition, ASSBs may enable higher energy densities by replacing the graphite anode in LIBs with an energy-dense Li-metal anode, increasing the battery capacity and voltage.[5–7] Finally, ASSBs enable the stacking of bipolar electrodes, reducing dead weight from casing, and improving the cell-level energy density.[8,9]

Numerous studies have focused on finding inorganic SEs enabling fast Li-ion transport (in the order of mS cm^{-1}),[2,10] with sulfides, oxides, and ternary halides amongst the most widely explored SEs. Sulfide SEs show high mechanical deformability, allowing for their implementation in ASSBs via simple cold-pressing processes.[3,11–13] However, sulfides exhibit poor oxidative (anodic) stability, reacting with high-voltage layered oxide positive electrode materials.[14–16] Oxide-based SEs exhibit wider electrochemical stability windows than sulfide SEs.[14,15] However, achieving sufficient Li-ion conductivities in oxides require dense pellets obtained through energy-intensive sintering processes, which are difficult to scale.[3,17] Additionally, the ionic conductivity of oxide SEs is typically lower than that of sulfide SEs.[11–13] Finally, ternary halide SEs, with formula Li_iMX_j (X= F, Cl, Br; i and j determined by the oxidation state of metal M) display high electrochemical oxidative stabilities (>4 V vs. Li/Li^+),[18–22] but are unstable against Li metal.[23]

From this analysis, it is evident that none of the SEs mentioned above can simultaneously provide adequate ionic conductivity and good chemical and electrochemical stability against the electrodes, as required to achieve viable ASSBs.[14,15,24,25] The inherent reactivity results in the formation of undesired decomposition products at the electrode/SE interfaces, creating additional interfaces and increasing the interfacial (contact) resistance for Li-ion conduction, with detrimental effects on battery performance.[5,16,24]

One practical strategy to solve this issue is to combine two SEs with different chemical and electrochemical stabilities to form bilayer composite separators.[16,26–28] In these composites, the anolyte is the SE in direct contact with the low voltage negative electrode material (*e.g.* graphite, or Li-metal, and its alloys), and the catholyte is the SE in contact with the high-voltage (typically, a layered oxide) positive electrode material.

Based on their electrochemical properties, sulfide, and oxide SEs are best employed as anolytes, whereas ternary halide SEs are well suited for catholyte applications. Several studies have claimed improved electrochemical performance of ASSBs using bilayer separators: Li_6PS_5Cl/Li_3InCl_6;[23,29–32] Li_6PS_5Cl/Li_3YCl_6;[27,33,34] Li_6PS_5Cl/Li_2ZrCl_6;[35–37] $Li_{10}GeP_2S_{12}$(LGPS)/Li

LGPS/Li_2ZrCl_6.[39] However, other investigations on similar bilayer based ASSBs have reported battery performance degradation enabled by specific SE pairings, such as Li_6PS_5Cl/Li_3InCl_6;[16,34,4
Li_6PS_5Cl/Li_3YCl_6;[42] Li_6PS_5Cl/Li_2ZrCl_6;[34] Li_3PS_4/Li_3InCl_6.[40] This degradation has been linked to the chemical incompatibility of specific anolyte and catholyte combinations with the formation of interfacial decomposition products. From these studies emerges the need to identify chemically compatible SEs to form stable and practical bilayer separators.
Screening with first-principles calculations, we analyze the thermodynamic chemical compatibility of an extensive range of inorganic materials, including oxide and sulfide SEs as anolytes and ternary halide SEs (chlorides and fluorides) as catholytes, for their potential use as bilayer separators in ASSBs. We find that Li_3PS_4 and Li_3PO_4 are the least reactive anolytes when in contact with halide catholytes. We identify a few bilayer interfaces that are thermodynamically stable upon contact. The Li_3PO_4/Li_3InCl_6 combination is examined experimentally for these few SE pairings that are predicted to be stable. Results from solid-state nuclear magnetic resonance (ssNMR), X-ray diffraction (XRD), X-ray photoelectron spectroscopy (XPS), and Raman spectroscopy suggest the excellent chemical compatibility of the Li_3PO_4/Li_3InCl_6 bilayer.

Methodology to Assess the Chemical Compatibility of Bilayer Separators

In this letter, we investigate two types of bilayer separators: sulfide/halide and oxide/halide combinations. Ternary halides, with formula Li_iMX_j (with X = Cl, and F) are always intended as the catholyte material. Table 1 shows the possible combinations of anolytes and catholytes considered in this study, totaling 72 distinct bilayer interfaces.
To efficiently survey the large compositional space covered by the material combinations of Table 1, we use first-principles calculations, based on density functional theory (DFT), to probe their thermodynamic stability upon contact, often referred to as "chemical sta-

Table 1: Materials used as catholyte and anolyte in this analysis. Starting from this list, all possible combinations of anolyte/catholyte are explored.

Catholytes	Anolytes
Chlorides: Li_2ZrCl_6, Li_3InCl_6, Li_2ZnCl_4, Li_3YCl_6, and $LiAlCl_4$	**Oxides:** Li_2O , Li_3PO_4, and $Li_7La_3Zr_2O_{12}$
Fluorides: Li_2ZrF_6, Li_3InF_6, $LiYF_4$, and Li_3AlF_6	**Sulfides:** Li_2S, Li_3P,* Li_3PS_4, Li_6PS_5Cl, and $Li_{10}Ge(PS_6)_2$

*Li_3P is included sulfide SEs.

bility".[46] Knowledge of the interfacial phase diagrams enable us to identify the relevant degradation reactions that may occur upon contact between anolytes and catholytes. For example, to investigate the chemical stability of Li_3PS_4 (anolyte) with Li_3InCl_6 (catholyte), we evaluated the Li-P-S-Cl-In quinary phase diagram. Using DFT, we computed the stability of all elements, as well as binary, ternary, quaternary, and unknown quinary compounds within this phase field, at ambient temperature and pressure.

Unless explicitly mentioned, we report the predicted chemical reactions and their enthalpies after implementing two thermodynamic corrections on the DFT data. The first correction deals with the computed formation energies (FEs) of oxygen and sulfur-containing compounds, affected by the significant systematic overbinding error for sulfur and oxygen molecules introduced by the generalized gradient approximation (GGA).[47,48] The second thermodynamic correction aligns the computed FEs with the experimental formation energies reported in the literature.[49,50] The chemical formulae of these compounds, and their experimental formation energies, are listed in Table S6. Reactions and enthalpies incorporating only the first correction are presented in Table S3 and Table S4.

In this extended search, we consider compounds from the Inorganic Crystal Structure Database (ICSD),[51] a set augmented by hypothetical phases from the Materials Project database[52] with metastability equal to or less than 30 meV/atom above the stability line (convex hull). For hypothetical compounds, we discard structures where volume changes upon DFT relaxation exceed 20%. Whenever possible, we consider polymorphs of compounds closely matching the structures reported in the ICSD as thermodynamically stable phases. The procedure to identify all possible decomposition reactions and their enthalpies

is described in further detail in the section "Bilayer Reactivity from First-principles Calculations".

The chemical stability of an interface is determined by evaluating the "spontaneity" of the reaction triggered upon contact of the anolyte and catholyte materials. Eq. 1 defines the decomposition reaction forming n decomposition products based on a given anolyte/catholyte pair. This reaction is accompanied by a reaction enthalpy ΔH in kJ mol^{-1} (implying one mole of total reactants). Thus, the spontaneity of Eq. 1 is entirely determined by the change in Gibbs free energy, which is approximated in the rest of this letter by ΔH. Thus, a decomposition reaction is spontaneous when $\Delta H < 0$, and more negative the value of ΔH, the greater the thermodynamic driving force for decomposition. We monitor the magnitude of ΔH as the main descriptor to quantify the chemical stability of an interface.

$$\text{anolyte} + \text{catholyte} \xleftrightarrow{\Delta H} \sum_{i=1}^{n} \text{product}_i \tag{1}$$

Here, we report the reaction with the predicted lowest (most negative) ΔH from the analysis of the appropriate multi-component phase diagram. Additional reactions with more positive ΔH values are tabulated in the Supporting Information (SI).

As an example of application of Eq. 1 to a real system, we consider the chemical reactivity of Li_3PS_4 as anolyte and Li_3InCl_6 as catholyte:

$$0.5\,Li_3PS_4\,(\text{anolyte}) + 0.5\,Li_3InCl_6\,(\text{catholyte}) \xrightarrow{\Delta H\ (-75\ \text{kJ mol}^{-1})} 0.5\,InPS_4 + 3\,LiCl \tag{2}$$

The reaction products resulting from Eq. 2 include a binary salt LiCl and a ternary thiophosphate $InPS_4$. Notably, the reaction presented in Eq. 2 is not a redox reaction, i.e., it does not involve a change in the oxidation states of the chemical species. It is instead a metathesis reaction. Further, the calculated reaction enthalpy of Eq. 2, $\Delta H = -75$ kJ mol^{-1} is substantial. In practice, the value of ΔH is computed from the difference between the FEs of products and reactants as $\Delta H = 3\times FE(LiCl) + 0.5\times FE(InPS_4) - 0.5\times FE(Li_3PS_4) - 0.5\times FE(Li_3InCl_6)$. Here, FE is intended as the energy change to form a compound from its elemental constituents in their stable states at ambient conditions (298 K and 1 atm); for example, the formation energy of LiCl is the energy change associated with the reac-

tion $Li(s) + Cl_2(g) \rightarrow LiCl(s)$. We note that the formation of quinary compounds based on Li–P–S–In–Cl, and with varying stoichiometries, were also considered. While we found no enthalpic gain in forming these quinary compounds upon mixing Li_3InCl_6 and Li_3PS_4 at room temperature (i.e., under typical battery operation conditions), such decomposition products may form at very high temperatures, due to entropic stabilization.

Reactivity of Sulfide Anolytes with Chloride Catholytes

We apply Eq. 1 to find all plausible decomposition reactions when mixing, pairs of sulfide anolytes and chloride catholytes listed in Table 1. Figure 1(a) shows the heatmap for their computed DFT reaction enthalpies ΔH (in kJ mol^{-1}).

From Figure 1(a), we observe that among the sulfide SEs, Li_3PS_4 shows the least reactivity with any of the ternary chlorides, with $Li_3PS_4/LiAlCl_4$ interface featuring as the least reactive. Sulfide anolytes show the mildest reactivity when in contact with $LiAlCl_4$ and Li_3YCl_6 chloride catholytes. In contrast, sulfide anolytes appear the most reactive with Li_3InCl_6.

Given that Li_2S and Li_3P are common decomposition products of sulfide electrolytes (*e.g.*, Li_6PS_5Cl, Li_3PS_4, and $Li_{10}Ge(PS_6)_2$ (LGPS)) at low potentials, for example, when in contact with Li-metal,[14,24,25,53] it is important to analyze the reactivity of these binary compounds (i.e., Li_2S and Li_3P) with the catholytes of interest. For Li_2S, the lowest and the highest reaction enthalpies vary between –58 kJ mol^{-1} and –89 kJ mol^{-1} for Li_3YCl_6 and Li_3InCl_6, respectively. Amongst the anolytes studied here, we find Li_3P to be the most reactive; the highest reactivity is observed when Li_3P is paired with Li_3InCl_6 (–236 kJ mol^{-1}), and the least reactivity is observed when it is paired with Li_3YCl_6 (–128 kJ mol^{-1}).

We next analyze the reactivity of the argyrodite electrolyte, Li_6PS_5Cl with the chloride catholytes listed in Table 1. Li_6PS_5Cl has a high Li-ion conductivity in the range of 1-10 mS cm^{-1} at room temperature,[54–56] and can be processed using a simple cold-pressing method, making it a viable SE for ASSBs.[57] Our results suggest that Li_6PS_5Cl reacts with

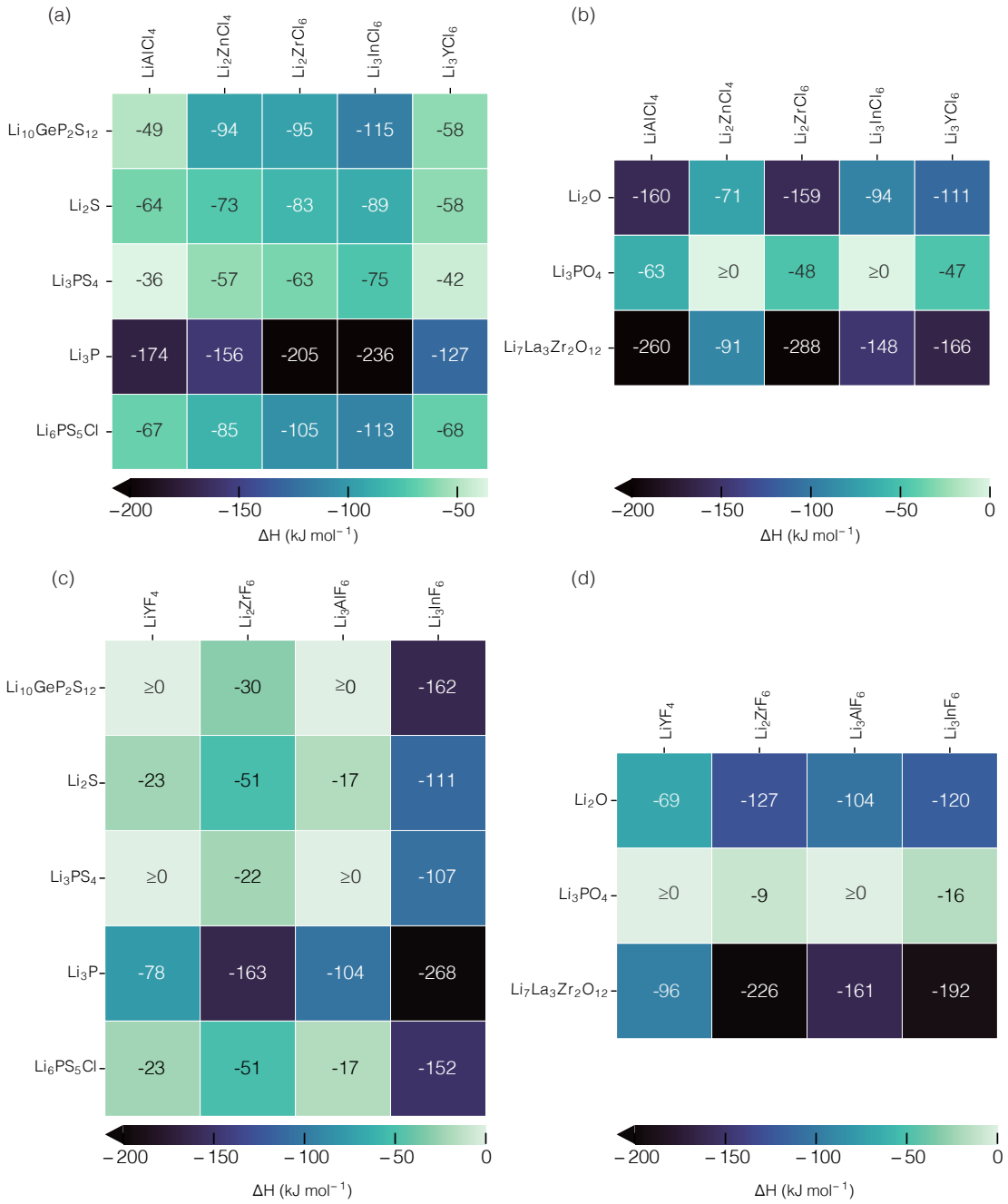

Figure 1: Chemical compatibility of anolytes and ternary chloride and fluoride catholytes (Li_iMX_j with X = F or Cl) in terms of computed ΔH (in kJ mol^{-1}).The anolytes are sulfides in panels (a) and (c) and are oxides in panels (b) and (d). The catholytes are chlorides in panels (a) and (b) and are fluorides in panels (c) and (d). ≥ 0 kJ mol^{-1} indicates absence of reactivity.

all of the chloride catholytes studied here, with $\Delta H \leq -67$ kJ mol^{-1}. LiCl always features as a major (defined in terms of the number moles of LiCl per reaction) decomposi-

tion product for all pairs of Li_6PS_5Cl and chloride catholytes. This observation is also true for all other sulfide anolytes studied here.

The most and least reactive pairs are shown in Eqs. 3 and 4:

$$0.6\,Li_3InCl_6 \;+\; 0.4\,Li_6PS_5Cl \xrightarrow{\Delta H\ (-113\ \text{kJ mol}^{-1})} 0.4\,InPS_4 \;+\; 0.2\,LiInS_2 \;+\; 4\,LiCl \tag{3}$$

$$0.6\,LiAlCl_4 \;+\; 0.4\,Li_6PS_5Cl \xrightarrow{\Delta H\ (-67\ \text{kJ mol}^{-1})} 0.2\,LiAlS_2 \;+\; 0.4\,AlPS_4 \;+\; 2.8\,LiCl \tag{4}$$

In addition to LiCl, reaction products include metal thiophosphates ($InPS_4$ and $AlPS_4$) and lithium metal sulfides ($LiInS_2$ and $LiAlS_2$). No change in the formal oxidation states of the elements occurs in Eqs. 3 and 4, classifying them as metathesis reactions.

Next, we extend this analysis to all bilayers formed between sulfides and chloride catholytes and use pie charts to represent the distribution of reaction products, as shown in Figure 2. This figure only reports the reactions with the most negative values of ΔH. Pie charts illustrating the reaction of LGPS and Li_3P (as anolytes) with chloride catholytes are in Figure S1 of the SI.

The pie charts in Figure 2 reveal that LiCl always accounts for at least 75 mol% of the reaction products. Interestingly, similar reaction products are observed from the metathesis reactions between sulfides (except LGPS) and Li_3InCl_6, Li_3YCl_6, or $LiAlCl_4$, as shown in Table S1 in the SI. This could be due to the common (3+) oxidation state of the transition metal in the chloride catholytes containing In, Y, or Al. In the case of LGPS, its reaction with Li_3InCl_6 is redox in nature, as revealed by the apparent changes in the oxidation states of the P (+5 in LGPS to +4 in $In_2(PS_3)_3$) and S (–2 in LGPS to –1 in P_2S_7) species.

Reactivity of Oxide Anolytes with Chloride Catholytes

We now consider the chemical compatibility of oxide anolytes with the chloride catholytes listed in Table 1. We include Li_2O in our list of oxides as it is a common decomposition product of many oxide SEs (*e.g.*, LLZO, and LiPON) when placed in contact with Li metal.[15,58]

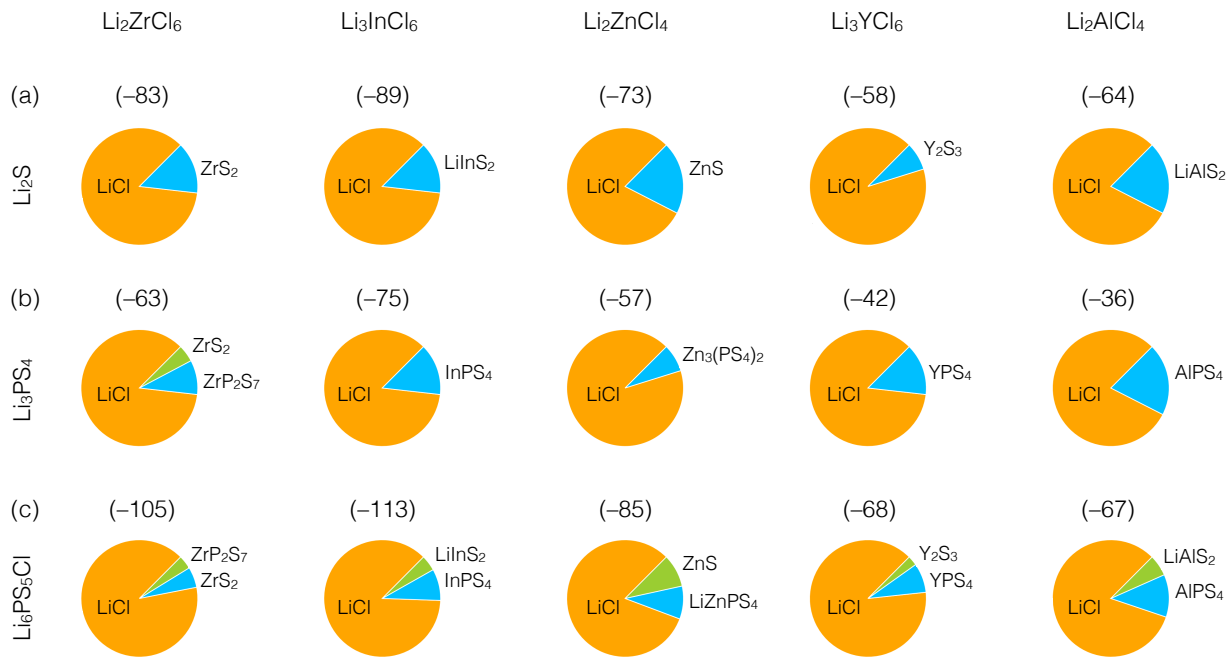

Figure 2: Predicted decomposition products when sulfide anolytes react chemically with chloride catholytes. Reaction enthalpies are reported above each pie chart (in round brackets) in kJ mol^{-1}. The area of each slice is proportional to the mole fraction of the products formed based on the stoichiometry of the reaction, assuming that the reaction goes to completion.

The heatmap of Figure 1(b) shows the predicted reaction enthalpies when these two material classes react. Among the oxides, Li_3PO_4 is the least reactive, and $Li_7La_3Zr_2O_{12}$ (LLZO) is the most reactive with the ternary chlorides. Oxide anolytes show the least reactivity with Li_2ZnCl_4, while they appear to be most reactive with $LiAlCl_4$ and Li_2ZrCl_6.
We now analyze the reactivity of LLZO with different chlorides, as LLZO is the most widely studied oxide SE. Our results suggest that LLZO is highly reactive with all of the chloride catholytes studied here, and LiCl consistently forms as a major decomposition product. This observation extends to all other oxide anolytes studied here. Eq. 5 and Eq. 6 high-

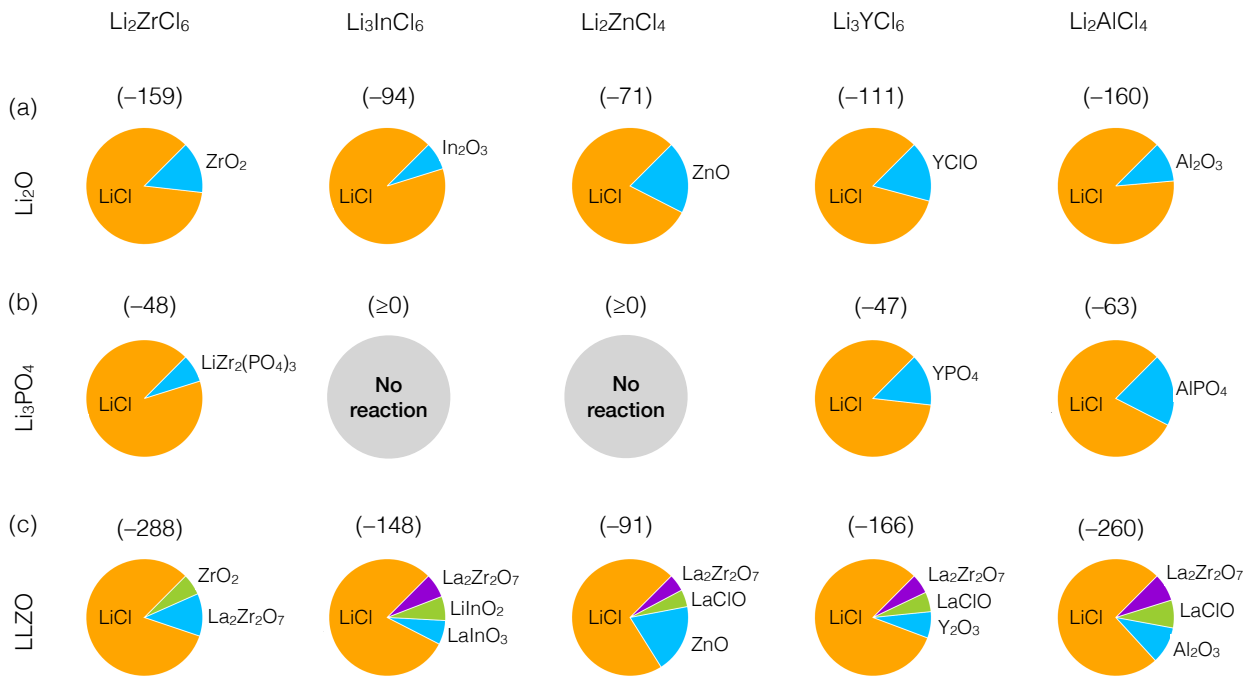

Figure 3: Predicted decomposition products when oxide anolytes react chemically with chloride catholytes. Reaction enthalpies are reported above each pie chart (in round brackets) in kJ mol^{-1}.

light the most and least reactive bilayer combinations with LLZO as the anolyte.

$$0.3636\,Li_7La_3Zr_2O_{12} + 0.6364\,Li_2ZrCl_6 \xrightarrow{\Delta H\ (-288\ kJ\ mol^{-1})} 0.5455\,La_2Zr_2O_7 + 0.2727\,ZrO_2 + 3.818\,LiCl \quad (5)$$

$$0.2\,Li_7La_3Zr_2O_{12} + 0.8\,Li_2ZnCl_4 \xrightarrow{\Delta H\ (-91\ kJ\ mol^{-1})} 0.2\,La_2Zr_2O_7 + 0.8\,ZnO + 0.2\,LaClO + 3\,LiCl \quad (6)$$

In both reactions (Eq. 5 and Eq. 6), LiCl appears as the primary decomposition product, while $La_2Zr_2O_7$ and metal oxides (ZrO_2 and ZnO) form as minor phases. Additionally, LaClO forms when LLZO reacts with Li_2ZnCl_4. Notably, LiCl, ZrO_2, and ZnO are all extremely stable binary compounds. There is no change in the formal oxidation states of the elements in Eq. 5 and Eq. 6, classifying them as metathesis reactions.

Next, we extend this analysis to all bilayers formed between oxides and chloride catholytes and once again use pie charts to represent the distribution of reaction products, as shown

in Figure 3. Unsurprisingly, LiCl is the major product (in terms of mole fraction). $La_2Zr_2O_7$ is another common product of the reaction between LLZO and each of the chloride SEs considered here. All reaction products shown in Figure 3 arise from metathesis reactions rather than redox ones. Notably, the Li_3PO_4/Li_2ZnCl_4 and Li_3PO_4/Li_3InCl_6 pairings are predicted to be thermodynamically stable on account of their positive ΔH values, and warrant further investigation. Hence, in the next section, we experimentally assess the chemical stability of one of these bilayer interfaces, namely Li_3PO_4/Li_3InCl_6, to test the validity of our predictions.

Experimental Investigation of the Li_3PO_4/Li_3InCl_6 Pairing

The chemical stability of Li_3InCl_6 and Li_3PO_4 was tested experimentally by heat-treating a mixture of the pure compounds and analyzing the product. The two SE powder samples were mixed in a 1:1 molar ratio and then pressed into pellets to ensure good contact between the SEs during subsequent heat treatment. One pellet was heat-treated at 300 °C for 24 hours inside a fused quartz tube sealed under vacuum to accelerate the reaction between the two compounds; the resulting product is denoted "Mixed 300 °C". Another pellet was placed inside a fused quartz tube under vacuum and left at 25 °C for 24 hours to mimic similar SE mixing conditions but without any heat treatment; the resulting product is referred to as "Mixed 25 °C". The Mixed pellets and the pure (unmixed) compounds were subsequently analyzed at room temperature using a combination of X-ray diffraction (XRD), solid-state nuclear magnetic resonance (ssNMR), and X-ray photoelectron spectroscopy (XPS).

The XRD patterns obtained on the Mixed samples exhibit significantly broader reflections than those obtained on the pure powders (see Figure S12). This broadening is at least in part due to a loss of crystallinity during the grinding step, as indicated by the

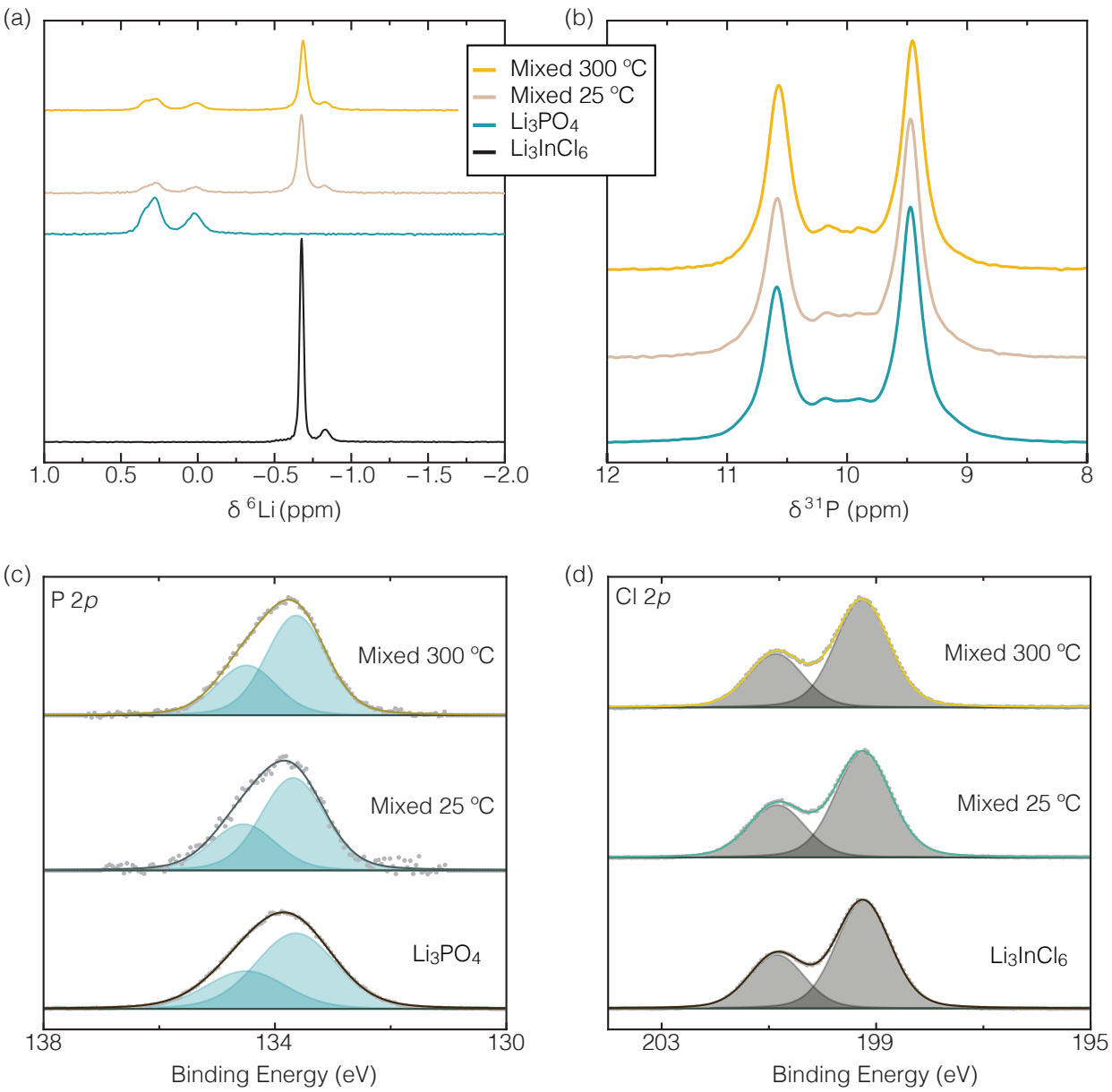

Figure 4: (a) ^{6}Li and (b) ^{31}P solid-state NMR spectra of Li_3InCl_6, Li_3PO_4, and the mixed and heat-treated samples. The spectra are scaled to maintain a constant total integrated intensity. All NMR data were collected using 30 kHz magic angle spinning at 18.8 T. High-resolution XPS spectra in the (c) P 2*p* and (d) Cl 2*p* regions for Li_3InCl_6, Li_3PO_4, and the mixed and heat-treated samples.

broadening of the peaks observed in the XRD patterns obtained on each of the pure compounds (Li_3InCl_6 and Li_3PO_4) after a similar grinding procedure (see Figure S14). Upon heat treatment of the Mixed 300 °C sample, the reflections corresponding to the Li_3InCl_6

and Li_3PO_4 phases sharpen, suggesting that some of the crystallinity is regained, but no new phases emerge (see Figure S12). The good stability of this electrolyte pairing is further confirmed by ^{6}Li and ^{31}P ssNMR. The spectra collected on the pure Li_3InCl_6 and Li_3PO_4 powder samples remain relatively unchanged after mixing at 25 °C, and even after a 300 °C heat treatment, as shown in Figure 4(a) and (b), respectively. A minor change in the occupancy of the P sites in Li_3PO_4 is evidenced by a change in the relative intensities of the signals in the "Mixed" ^{31}P spectra in Figure 4(b). Regarding the ^{6}Li data in Figure 4(a), the most intense signal in the two Mixed spectra, corresponding to Li species in the Li_3InCl_6 phase, is significantly broadened. This broadening is presumably due to an increase in the distribution of Li local environments (resulting in a narrow distribution of chemical shifts), in turn, caused by positional disorder in the Li_3InCl_6 structure induced upon grinding the powders together. Structural disordering is also observed when grinding Li_3InCl_6 alone, as shown in Figure S14. The lack of significant change in the ^{6}Li and ^{31}P NMR spectra collected on the Mixed 25 °C and Mixed 300 °C samples confirm that the Li_3InCl_6 and Li_3PO_4 phases are stable after heat treatment, with no new Li- or P-containing new phase (neither crystalline nor amorphous) formed. The P $2p$ and Cl $2p$ XPS spectra obtained on the pure compounds and the Mixed samples are presented in Figures 4(c) and (d), respectively. Figure S13 shows the Li $1s$ and In $3d$ XPS spectra for the unmixed and mixed samples. Similar XPS peaks are observed in all samples considered. Taken together, the XRD, ssNMR, and XPS analyses confirm the excellent chemical compatibility of Li_3InCl_6 with Li_3PO_4 predicted with our computational framework.

Reactivity of Sulfide and Oxide Anolytes with Fluoride Catholytes

Finally, we evaluate the chemical compatibility of sulfide and oxide anolytes with the fluoride catholytes listed in Table 1. Figures 1 (c) and (d) show the heatmaps for their reac-

tion enthalpies. It can be observed that Li_3PS_4 (among the sulfides) and Li_3PO_4 (among the oxides) show the mildest reactivity, i.e., the best chemical compatibility, with the fluoride catholytes. The sulfide and oxide anolytes show the least reactivity with $LiYF_4$ and Li_3AlF_6. In contrast, the oxide anolytes appear most reactive with Li_3InF_6. The reaction products are shown as pie charts in Figure S5—S7 of the SI. We note that, for the fluoride catholytes, the ΔH and the reaction products do not change significantly upon applying the second thermodynamic correction to the DFT results. Thus, this second correction is ignored. We find that bilayer interfaces with Li_3PS_4, LGPS, Li_3PO_4 as anolytes and $LiYF_4$, Li_3AlF_6 as catholytes have positive ΔH. Thus, these six interfaces are predicted to be chemically compatible.

Discussion

The experimental identification of viable bilayer interfaces and the experimental characterization of reactive (decomposing) bilayer interfaces in ASSBs remains a major challenge due to their buried nature.[3,25] Computational materials science enables us to perform an extensive screening of potential material combinations forming a bilayer interface, thereby providing a birds-eye view of this complex interfacial (and device) optimization problem. We analyzed the chemical compatibility of anolytes and catholytes forming a bilayer separator for ASSBs using a thermodynamic framework relying on first-principles calculations. Reaction enthalpies were used as descriptors to quantify the chemical compatibility of bilayer separators. For one representative bilayer interface, Li_3PO_4/Li_3InCl_6, our computational results predicting their good chemical compatibility were confirmed experimentally. While the preliminary step of computational screening using DFT calculations offers numerous advantages, these calculations are performed at 0 K, thus overlooking the entropic contributions to the chemical reactions. Considering entropic effects (vibrational and configurational) could change the predicted spontaneity of specific chemical reactions, partic-

ularly under moderate- to high-temperature conditions. Notably, DFT calculations predict the behavior of bilayer separators at thermodynamic equilibrium. However, the stability of the interface relies significantly on the kinetics of decomposition reactions, an aspect not considered by the theoretical treatments applied here.

We now compare the reaction products predicted herein to those reported previously when studying bilayer electrolyte cells. Starting with the sulfide/chloride pairings, Rosenbach et al.[16] studied the Li_6PS_5Cl/Li_3InCl_6 interface using time-of-flight secondary ion mass spectroscopy and focused ion beam scanning electron microscopy, and detected the formation of an InS^- chemical feature, potentially linked to In_2S_3 or $LiInS_2$. Studying the same interface, Lee et al.[44] also identified In_2S_3, PS_4^{3-}, P_2S_5 signatures by XPS. These reports indicate the instability of this bilayer.[16,44] The predictions for the Li_6PS_5Cl/Li_3InCl_6 interface in this work identified similar decomposition products (Eq. 3, Figure 2, Table S1, Table S3), such as $InPS_4$, $LiInS_2$, In_2S_3, and LiCl.

Koç et al.[41] reported the formation of LiCl as one of the decomposition products between Li_6PS_5Cl/Li_3InCl_6 and Li_3PS_4/Li_3InCl_6 interfaces, and hypothesized that the chemical instability of these bilayer interfaces caused the observed degradation in battery performance. The electrochemical performance was improved by adding a nanometer-thick layer of Li_3PO_4 in between Li_6PS_5Cl (anolyte) and a composite positive electrode (Li_3InCl_6 with NMC622 as active material, and binders).[41] They thus inferred the stability of the Li_3PO_4/Li_3InCl_6 interface, which was verified here by our theoretical predictions (Figure 1(b) and Figure 3) and further confirmed experimentally using various characterization techniques. For bilayer separators comprising a chloride catholyte, our simulations shortlisted only two thermodynamically stable interfaces: Li_3PO_4/Li_2ZnCl_4, and Li_3PO_4/Li_3InCl_6. Several observations can be made when comparing the chemical compatibility of the anolytes with the fluoride and chloride catholytes investigated here. (*i*) Similar reactivity trends are observed for these two classes of catholytes. For example, Li_3PS_4 and Li_3PO_4 show the best chemical compatibility (out of all the sulfide and oxide anolytes considered here)

with both chloride and fluoride-based catholytes. In contrast, sulfide anolytes show the highest reactivity with the In-containing Li_3InF_6 and Li_3InCl_6 catholytes. (*ii*) For those bilayer separators predicted to react, we also find that the reaction products from fluoride catholytes are similar to those from chloride catholytes. We have demonstrated that LiCl is a major product in the decomposition reactions involving chloride-containing catholytes. Similarly, LiF is a major decomposition product for all reacting fluoride-based bilayers. Except for LGPS, pairing sulfide anolytes with chloride or fluoride-containing catholytes leads to a metathesis decomposition reaction.

Having established a parallel between the reactivity trends of chloride and fluoride catholytes, we compare their stability against sulfide and oxide anolytes in terms of predicted ΔH values. Differences in ΔH values for fluoride and chloride catholytes are governed almost entirely by two main contributions: (i) On the product side of Eq. 1: the difference in FEs between LiCl and LiF. (ii) On the reactant side: the difference in FEs between Li_iMCl_j and Li_iMF_j. The FEs of LiF and Li_iMF_j compounds are more negative than their chloride analogs, which is justified by the higher electronegativity of fluorine ($\sim$3.98 according to the Pauling scale)[59] compared to chlorine ($\sim$3.16). Since LiF is a reaction product, its more negative FE makes the ΔH values of fluoride catholytes more negative (lower) –i.e., the reaction is more thermodynamically favorable– as compared to chlorides. On the other hand, the more negative FE of Li_iMF_j increases their ΔH (more positive values) compared to their chloride analogs. The competing effects of the more negative FEs of LiF and Li_iMF_j regulate the propensity to decompose fluoride-based bilayer separators. We find that only Li_3InF_6-based bilayers have more negative ΔH values (making it less stable) as compared to Li_3InCl_6-based bilayers (Figure 1). All other fluoride-based bilayers considered here have more positive ΔH values than their chloride analogs, making them more stable.

This analysis suggests that considering the chemical compatibility of bilayer separators is vital when pairing SEs. However, the integrity of the bilayer separator is only preserved

when the cell is operated within the electrochemical stability window (ESW) defined for bilayers by the reductive and oxidative potentials of the anolyte and catholyte, respectively. Outside the ESW, the SE may react and eventually decompose into other thermodynamically stable products.[15,58,60]

In the case of the Li_3PO_4/Li_3InCl_6 bilayer investigated here, Li_3PO_4 displays a reductive potential as low as ∼0.7 vs. Li/Li^+, whereas Li_3InCl_6 has a high oxidative potential ∼4.3 vs. Li/Li^+ (see computed values in Figure S10). Thus, the union of the anolyte Li_3PO_4 reducing potential and the catholyte Li_3InCl_6 oxidative potentials defines the ESW of the bilayer separator, which occurs in the 0.7–4.3 V vs. Li/Li^+ range. Outside the 0.7–4.3 V voltage range, at least one SE is expected to decompose into simpler thermodynamically stable compounds at the corresponding potential.

Conclusions

The development of viable all-solid-state batteries is limited by the lack of solid electrolytes that are simultaneously stable in contact with both the high-voltage cathode and low-voltage anode. Bilayer separators could potentially mitigate this issue, provided the constituent materials are chemically compatible.

Using a robust thermodynamic framework powered by first-principles calculations, we investigated the chemical compatibility of 72 bilayer interfaces formed between halide catholytes and several types of anolytes, including sulfides or oxides.

Among all the anolytes studied, Li_3PS_4 (among sulfides) and Li_3PO_4 (among oxides) demonstrated the least reactivity with ternary halide catholytes. Our simulations identified a subset of bilayer separators with substantial chemical compatibility, making them potential candidates for use in ASSBs. In-depth experimental characterization of the Li_3PO_4/Li_3InCl_6 bilayer combination confirmed the innate chemical stability of this interface. This study underlines the importance of understanding the chemical stability of SE interfaces in bi-

layer ASSBs.

Bilayer Reactivity from First-principles Calculations

We used density functional theory (DFT) to compute the reaction enthalpies ΔHs of several important chemical reactions investigated in this work. In DFT, wavefunctions were described using plane waves for valence electrons and projected augmented wave potentials for the core electrons, as implemented in the Vienna Ab initio Simulation Package.[61,62] The unknown exchange and correlation contribution was approximated by the generalized gradient approximation (GGA) by Perdew, Burke, and Ernzerhof (PBE).[63] The parameters used for geometry optimization and energy calculations follow the MITRelaxSet, as in Ref. 64. We used a plane wave energy cut-off of 520 eV, and the total energy was converged to 10^{-5} eV per cell. Geometries (coordinates, volumes, and cell shapes) were considered converged when the total energy difference between two consecutive geometry steps was lower than 10^{-4} eV (per cell).

Predictions using GGA functionals are typically affected by a significant systematic overbinding error for sulfur and oxygen molecules when calculating the formation energies of oxygen and sulfur-containing compounds. Consequently, the calculated formation energies of oxygen and sulfur-containing compounds with GGA appear fictitiously more positive (by a constant value) than their reference experimental formation energies.[47,48] We use the oxygen corrections as already implemented in Ref. 64. For the sulfur-containing compounds, we fit the experimental formation energies of several binary sulfides as available in the Ref. 49 against their computed formation energies with GGA (Figure S11). These corrections were applied systematically to all compounds containing oxygen and sulfur atoms in their formulae.

Whenever experimental formation energies[49,50] of compounds considered in this investigation are reported, we correct their DFT total energies to match the experimental forma-

tion energies reported in the literature. These corrections are tabulated in Table S6. Thus, all reactions reported in this letter include both overbinding and experimental corrections. We also report reactions without the experimental corrections in Table S3 and Table S4, as well as in Figure S2—S4, Figure S8—S9.

The reaction enthalpies and viable chemical reactions were accessed using multi-component phase diagrams based on first-principles DFT calculations. For the construction of these phase diagrams, we use the methodology exposed in Ref. 65. We assume that the two materials combined into a heterogeneous interface may react to form products under thermodynamic equilibrium. In particular, consider an arbitrary reaction of the type $xc_a + (1-x)\,c_b \;\rightarrow\; \sum c_{eqm}$ where x is the fraction of material a with composition c_a reacts with $(1-x)$ of b with composition c_b, to give reaction products $\sum c_{eqm}$ under conditions of thermodynamic equilibrium. The reaction products are determined by constructing a pseudo-binary phase diagram between the two materials and calculating the reaction enthalpies for all possible x, given by Eq. 7.

$$\Delta H\left[c_a, c_b\right] = \min_{x\in[0,\ 1]} \left\{ H_{eq}\left[xc_a + (1-x)\,c_b\right] - xH\left[c_a\right] - (1-x)\,H\left[c_b\right] \right\}. \tag{7}$$

where $\Delta H\left[c_a, c_b\right]$ is the reaction enthalpy for the interface of two phases a and b with compositions c_a and c_b. $H_{eq}\left[c\right]$ is the enthalpy of the phase equilibria at composition c, determined from the phase diagram. $H\left[c_a\right]$ and $H\left[c_b\right]$ are the enthalpies of phases a and b respectively. Note, in the DFT calculations, we neglected the $p\Delta$V term in determining ΔH, and thus all enthalpy terms of Eq 7 are approximated by the DFT total energies.

The spontaneity of a reaction is entirely determined by the change in Gibbs free energy. Since DFT calculations are conducted at 0 K without considering entropy effects, $\Delta H\left[c_a, c_b\right]$ of Eq. 7 can be approximated as a descriptor for the spontaneity of the reaction between two materials a and b. Thus, the more negative the quantity $\Delta H\left[c_a, c_b\right]$, the greater the thermodynamic driving force for the interface to decompose into $\sum c_{eqm}$.

Experimental Methods

Sample preparation

Li_3PO_4 was purchased from Sigma-Aldrich with purity $\geq 98\%$. Li_3InCl_6 was mechanochemically synthesized from LiCl (99+%, Sigma-Aldrich) and $InCl_3$ (99.999+%, Sigma-Aldrich). All preparation was performed inside an argon atmosphere. Powders were mixed at a stoichiometric ratio with a 10% excess of $InCl_3$ to account for its preferential adhesion to the agate mortar and pestle. The powders were hand-ground for 15 minutes with breaks to scrape off the adhered powder. The mixture was then loaded into a zirconia jar with fifteen 10 mm Y-stabilized zirconia spherical grinding media and sealed using parafilm. The mixture was ball-milled at 500 rpm in cycles of 15 minutes milling followed by 1 minute rest for a total of 3 hours using a high-energy planetary ball mill (Retsch PM 200). Li_3InCl_6 and Li_3PO_4 powders were each pressed into 175 mg pellets using a 6 mm stainless steel die set under 9.1 kN of force in a hydraulic press. Pellets were each sealed inside a fused quartz tube under vacuum and subsequently heat treated at 300 °C for 12 hours in a tube furnace (Thermo-Scientific Lindberg Blue M) ending with an air quench. The quartz tubes were previously dried in a vacuum oven at approximately 225°C for 12 hours. Both pellets were then briefly crushed into a powder using an agate mortar and pestle. Mixed-electrolyte samples were made by hand-grinding a 1:1 molar mixture of heat-treated Li_3InCl_6 and Li_3PO_4 powders in an agate mortar for 15 minutes with breaks from scraping adhered powder. As described above, two pellets of approximately 50 mg were made from the mixture and sealed into fused quartz tubes. One pellets was heat-treated in the tube furnace at 300 °C for 24 hours and air-quenched. These pellets were also crushed into powder form using an agate mortar and pestle.

Characterization methods

X-ray diffraction (XRD)

XRD measurements were taken using a PANalytical Empyrean Powder Diffractometer in reflection geometry with a Cu Kα source. Samples were prepared by evenly spreading approximately 20 mg of powder into the wells of silicon crystal zero-diffraction plates (MTI Corporation) and sealing them into custom air-free cells with Kapton windows. Data were acquired using an average of 6 scans over a total of 30 minutes, confirming no trends in peak height between scans to ensure no air exposure occurred.

Solid-state nuclear magnetic resonance (ssNMR)

NMR data were collected using an 18.8 T (800 MHz for ^{1}H) MHz Bruker Ultrashield Plus standard bore magnet equipped with an Avance III console. Samples were packed into 2.5 mm zirconia rotors under an argon atmosphere and covered with small amounts of PTFE tape to protect from air exposure. Rotors were spun using dry nitrogen at 30 kHz in a 2.5 mm HX MAS probe.

^{6}Li measurements were taken using a 90-degree flip angle with 3.34 μs pulse length at 200 W power with a 300 s recycle delay for Li_3InCl_6 and a 2400 s recycle delay for other samples. Chemical shifts were calibrated using 1M LiCl at 0 ppm. ^{31}P measurements were taken using a 90-degree flip angle with 1.52 μs pulse length at 200 W power with a 2400 s recycle delay for Li_3PO_4 and a 2250 s recycle delay for other samples. Chemical shifts were calibrated with 1M H_3PO_4 at 0 ppm. Spectra were processed with TopSpin 3.6 without line broadening.

X-ray photoelectron spectroscopy (XPS)

XPS samples were prepared under an argon atmosphere and attached to a custom air-free stage using carbon adhesive discs. Measurements were acquired using a ThermoFisher Es-

calab Xi+ instrument with 1486.68 eV monochromated X-rays from an Al anode X-ray source using a flood gun for charge compensation. Survey scans were initially acquired with a 50 ms dwell time, 100 eV pass energy, and averaging over 4 scans. High-resolution scans were then taken of C 1s, Cl 2p, In 3d, Li 1s, O 1s, and P 2p regions according to their positions in the survey data. These scans used a dwell time of 50 ms, pass energy of 20 eV, and averaged a varying number of scans depending on the signal intensity.
The collected data were analyzed and fit with the CasaXPS software using 'W Tougaard' or 'Shirley' backgrounds as appropriate. The binding energy scale was calibrated by assigning the adventitious carbon peak to 248.8 eV. The Li_3PO_4 sample was further shifted by +.3825 eV to account for a different background under its adventitious carbon peak by aligning it with shared peaks in other regions.

Acknowledgement

P. C. acknowledges funding from the National Research Foundation under NRFF12-2020-0012 program, Singapore. The computational work was performed on resources of the National Supercomputing Centre, Singapore (https:// www.nscc.sg). We acknowledge the Robert A. Welch Foundation for Pieremanuele Canepa Welch's Professorship at the Texas Center for Superconductivity. This work used the shared facilities of the Materials Research Science and Engineering Center (MRSEC) at UC Santa Barbara: NSF DMR–2308708. The UC Santa Barbara MRSEC is a member of the Materials Research Facilities Network (www.mrfn.com). This work was supported by LG Energy Solution—UC San Diego Frontier Research Laboratory via the Open Innovation program. The authors acknowledge using the Laboratory for Surface Characterization within the California NanoSystems Institute, supported by the University of California, Santa Barbara, and the University of California, Office of the President. This material is based upon work supported by the National Science Foundation Graduate Research Fellowship Program under Grant Nos.

1650114 and 2139319. Any opinions, findings, conclusions, or recommendations expressed in this material are those of the author(s) and do not necessarily reflect the views of the National Science Foundation.

Supporting Information Available

The Supporting Information is available free of charge at $\cdots$.

Computed Reaction energies of anolytes (halides) and catholytes (oxides and sulfides) with multiple thermodynamic corrections. Phase stability of ternary halides. List of experimental formation energy of binary, ternary compounds. Computed electrochemical stability windows of bilayer separators. X-ray diffractograms, XPS, and ^{6}Li ssNMR spectra of Li_3InCl_6, Li_3PO_4, and their mixtures at various conditions.

References

(1) Tian, Y.; Zeng, G.; Rutt, A.; Shi, T.; Kim, H.; Wang, J.; Koettgen, J.; Sun, Y.; Ouyang, B.; Chen, T.; Lun, Z.; Rong, Z.; Persson, K.; Ceder, G. Promises and Challenges of Next-Generation "Beyond Li-ion" Batteries for Electric Vehicles and Grid Decarbonization. *Chem. Rev.* **2021**, *121*, 1623–1669.

(2) Bachman, J. C.; Muy, S.; Grimaud, A.; Chang, H.-H.; Pour, N.; Lux, S. F.; Paschos, O.; Maglia, F.; Lupart, S.; Lamp, P.; Giordano, L.; Shao-Horn, Y. Inorganic Solid-State Electrolytes for Lithium Batteries: Mechanisms and Properties Governing Ion Conduction. *Chem. Rev.* **2016**, *116*, 140–162.

(3) Famprikis, T.; Canepa, P.; Dawson, J. A.; Islam, M. S.; Masquelier, C. Fundamentals of Inorganic Solid-State Electrolytes for Batteries. *Nat. Mater.* **2019**, *18*, 1278–1291.

(4) Janek, J.; Zeier, W. G. Challenges in Speeding up Solid-State Battery Development. *Nat. Energy* **2023**, *8*, 230–240.

(5) Krauskopf, T.; Richter, F. H.; Zeier, W. G.; Janek, J. Physicochemical Concepts of the Lithium Metal Anode in Solid-State Batteries. *Chem. Rev.* **2020**, *120*, 7745–7794.

(6) Manthiram, A.; Yu, X.; Wang, S. Lithium Battery Chemistries Enabled by Solid-State Electrolytes. *Nat. Rev. Mater.* **2017**, *2*, 16103.

(7) Janek, J.; Zeier, W. G. A Solid Future for Battery Development. *Nat. Energy* **2016**, *1*, 1–4.

(8) Nam, Y. J.; Cho, S.-J.; Oh, D. Y.; Lim, J.-M.; Kim, S. Y.; Song, J. H.; Lee, Y.-G.; Lee, S.-Y.; Jung, Y. S. Bendable and thin sulfide solid electrolyte film: a new electrolyte opportunity for free-standing and stackable high-energy all-solid-state lithium-ion batteries. *Nano letters* **2015**, *15*, 3317–3323.

(9) Kato, Y.; Hori, S.; Saito, T.; Suzuki, K.; Hirayama, M.; Mitsui, A.; Yonemura, M.; Iba, H.; Kanno, R. High-Power All-Solid-State Batteries Using Sulfide Superionic Conductors. *Nat. Energy* **2016**, *1*, 1–7.

(10) Tufail, M. K.; Zhai, P.; Jia, M.; Zhao, N.; Guo, X. Design of Solid Electrolytes with Fast Ion Transport: Computation-Driven and Practical Approaches. *Energy Material Advances* **2023**, *4*, 0015.

(11) Park, K. H.; Bai, Q.; Kim, D. H.; Oh, D. Y.; Zhu, Y.; Mo, Y.; Jung, Y. S. Design Strategies, Practical Considerations, and New Solution Processes of Sulfide Solid Electrolytes for All-Solid-State Batteries. *Advanced Energy Materials* **2018**, *8*, 1800035.

(12) Xiao, Y.; Wang, Y.; Bo, S.-H.; Kim, J. C.; Miara, L. J.; Ceder, G. Understanding Interface Stability in Solid-State Batteries. *Nat. Rev. Mater.* **2020**, *5*, 105–126.

(13) Kwak, H.; Wang, S.; Park, J.; Liu, Y.; Kim, K. T.; Choi, Y.; Mo, Y.; Jung, Y. S.

Emerging Halide Superionic Conductors for All-Solid-State Batteries: Design, Synthesis, and Practical Applications. *ACS Energy Letters* **2022**, *7*, 1776–1805.

(14) Richards, W. D.; Miara, L. J.; Wang, Y.; Kim, J. C.; Ceder, G. Interface Stability in Solid-State Batteries. *Chem. Mater.* **2016**, *28*, 266–273.

(15) Zhu, Y.; He, X.; Mo, Y. Origin of Outstanding Stability in the Lithium Solid Electrolyte Materials: Insights from Thermodynamic Analyses Based on First-Principles Calculations. *ACS Appl. Mater. Interfaces* **2015**, *7*, 23685–23693.

(16) Rosenbach, C.; Walther, F.; Ruhl, J.; Hartmann, M.; Hendriks, T. A.; Ohno, S.; Janek, J.; Zeier, W. G. Visualizing the Chemical Incompatibility of Halide and Sulfide-Based Electrolytes in Solid-State Batteries. *Adv. Energy Mater.* **2023**, *13*, 2203673.

(17) Allen, J.; Wolfenstine, J.; Rangasamy, E.; Sakamoto, J. Effect of substitution (Ta, Al, Ga) on the conductivity of $Li_7La_3Zr_2O_{12}$. *J. Power Sources* **2012**, *206*, 315–319.

(18) Li, X.; Liang, J.; Yang, X.; Adair, K. R.; Wang, C.; Zhao, F.; Sun, X. Progress and Perspectives on Halide Lithium Conductors for All-Solid-State Lithium Batteries. *Energy Environ. Sci.* **2020**, *13*, 1429–1461.

(19) Asano, T.; Sakai, A.; Ouchi, S.; Sakaida, M.; Miyazaki, A.; Hasegawa, S. Solid Halide Electrolytes with High Lithium-Ion Conductivity for Application in 4 V Class Bulk-Type All-Solid-State Batteries. *Adv. Mater.* **2018**, *30*, 1803075.

(20) Li, X. et al. Air-Stable Li_3InCl_6 Electrolyte with High Voltage Compatibility for All-Solid-State Batteries. *Energy Environ. Sci.* **2019**, *12*, 2665–2671.

(21) Li, X.; Liang, J.; Chen, N.; Luo, J.; Adair, K. R.; Wang, C.; Banis, M. N.; Sham, T.-K.; Zhang, L.; Zhao, S.; Lu, S.; Huang, H.; Li, R.; Sun, X. Water-Mediated Synthesis of a Superionic Halide Solid Electrolyte. *Angew. Chem.* **2019**, *131*, 16579–16584.

(22) Sebti, E.; Evans, H. A.; Chen, H.; Richardson, P. M.; White, K. M.; Giovine, R.; Koirala, K. P.; Xu, Y.; Gonzalez-Correa, E.; Wang, C.; Brown, C. M.; Cheetham, A. K.; Canepa, P.; Clément, R. J. Stacking Faults Assist Lithium-Ion Conduction in a Halide-Based Superionic Conductor. *J. Am. Chem. Soc.* **2022**, *144*, 5795–5811.

(23) Riegger, L. M.; Schlem, R.; Sann, J.; Zeier, W. G.; Janek, J. Lithium-Metal Anode Instability of the Superionic Halide Solid Electrolytes and the Implications for Solid-State Batteries. *Angew. Chem. Int. Ed.* **2021**, *60*, 6718–6723.

(24) Wenzel, S.; Sedlmaier, S. J.; Dietrich, C.; Zeier, W. G.; Janek, J. Interfacial Reactivity and Interphase Growth of Argyrodite Solid Electrolytes at Lithium Metal Electrodes. *Solid State Ionics* **2018**, *318*, 102–112.

(25) Wang, J.; Panchal, A. A.; Sai Gautam, G.; Canepa, P. The Resistive Nature of Decomposing Interfaces of Solid Electrolytes with Alkali Metal Electrodes. *J. Mater. Chem. A* **2022**, *10*, 19732–19742.

(26) Kochetkov, I.; Zuo, T.-T.; Ruess, R.; Singh, B.; Zhou, L.; Kaup, K.; Janek, J.; Nazar, L. Different Interfacial Reactivity of Lithium Metal Chloride Electrolytes with High Voltage Cathodes Determines Solid-State Battery Performance. *Energy Environ. Sci.* **2022**, *15*, 3933–3944.

(27) Wang, C.; Liang, J.; Luo, J.; Liu, J.; Li, X.; Zhao, F.; Li, R.; Huang, H.; Zhao, S.; Zhang, L.; Wang, J.; Sun, X. A Universal Wet-Chemistry Synthesis of Solid-State Halide Electrolytes for All-Solid-State Lithium-Metal Batteries. *Sci. Adv.* **2021**, *7*, eabh1896.

(28) Zhou, L.; Zuo, T.-T.; Kwok, C. Y.; Kim, S. Y.; Assoud, A.; Zhang, Q.; Janek, J.; Nazar, L. F. High Areal Capacity, Long Cycle Life 4 V Ceramic All-Solid-State Li-ion Batteries Enabled by Chloride Solid Electrolytes. *Nat. Energy* **2022**, *7*, 83–93.

(29) Hendriks, T. A.; Lange, M. A.; Kiens, E. M.; Baeumer, C.; Zeier, W. G. Balancing Partial Ionic and Electronic Transport for Optimized Cathode Utilization of High-Voltage $LiMn_2O_4/Li_3InCl_6$ Solid-State Batteries. *Batteries & Supercaps* **2023**, *6*, e202200544.

(30) Kim, Y.; Juarez-Yescas, C.; Liao, D. W.; Jangid, M. K.; Joshi, P.; Yang, H.; Zahiri, B.; Braun, P. V.; Dasgupta, N. P. Thin Free-Standing Sulfide/Halide Bilayer Electrolytes for Solid-State Batteries Using Slurry Processing and Lamination. *ACS Energy Lett.* **2024**, *9*, 1353–1360.

(31) Wang, C.; Yu, R.; Duan, H.; Lu, Q.; Li, Q.; Adair, K. R.; Bao, D.; Liu, Y.; Yang, R.; Wang, J.; Zhao, S.; Huang, H.; Sun, X. Solvent-Free Approach for Interweaving Free-standing and Ultrathin Inorganic Solid Electrolyte Membranes. *ACS Energy Lett.* **2022**, *7*, 410–416.

(32) Jin, F.; Fadillah, L.; Nguyen, H. Q.; Sandvik, T. M.; Liu, Y.; García-Martín, A.; Salagre, E.; Michel, E. G.; Stoian, D.; Marshall, K.; others Elucidating the Impact of Li3InCl6-Coated LiNi0. 8Co0. 15Al0. 05O2 on the Electro-Chemo-Mechanics of Li6PS5Cl-Based Solid-State Batteries. *Chemistry of Materials* **2024**,

(33) Ji, W.; Zheng, D.; Zhang, X.; Ding, T.; Qu, D. A Kinetically Stable Anode Interface for Li_3YCl_6-Based All-Solid-State Lithium Batteries. *J. Mater. Chem. A* **2021**, *9*, 15012–15018.

(34) Samanta, S.; Bera, S.; Biswas, R. K.; Mondal, S.; Mandal, L.; Banerjee, A. Ionocovalency of the Central Metal Halide Bond-Dependent Chemical Compatibility of Halide Solid Electrolytes with Li6PS5Cl. *ACS Energy Letters* **2024**, *9*, 3683–3693.

(35) Luo, X.; Zhong, Y.; Wang, X.; Xia, X.; Gu, C.; Tu, J. Ionic Conductivity Enhancement of Li2ZrCl6 Halide Electrolytes via Mechanochemical Synthesis for All-Solid-State Lithium–Metal Batteries. *ACS Appl. Mater. Interfaces* **2022**, *14*, 49839–49846.

(36) Zhang, H.; Yu, Z.; Cheng, J.; Chen, H.; Huang, X.; Tian, B. Halide/Sulfide Composite Solid-State Electrolyte for Li-anode Based All-Solid-State Batteries. *Chin. Chem. Lett.* **2023**, *34*, 108228.

(37) Wang, K.; Ren, Q.; Gu, Z.; Duan, C.; Wang, J.; Zhu, F.; Fu, Y.; Hao, J.; Zhu, J.; He, L.; Wang, C.-W.; Lu, Y.; Ma, J.; Ma, C. A Cost-Effective and Humidity-Tolerant Chloride Solid Electrolyte for Lithium Batteries. *Nat. Commun.* **2021**, *12*, 4410.

(38) Luo, X.; Cai, D.; Wang, X.; Xia, X.; Gu, C.; Tu, J. A Novel Ethanol-Mediated Synthesis of Superionic Halide Electrolytes for High-Voltage All-Solid-State Lithium–Metal Batteries. *ACS Appl. Mater. Interfaces* **2022**, *14*, 29844–29855.

(39) Shi, J.; Yao, Z.; Xiang, J.; Cai, C.; Tu, F.; Zhang, Y.; Yao, W.; Jia, Q.; Zhou, Y.; Shen, S.; Yang, Y. High-Conductivity Li $_2$ ZrCl $_6$ Electrolytes via an Optimized Two-Step Ball-Milling Method for All-Solid-State Lithium–Metal Batteries. *ACS Sustainable Chem. Eng.* **2024**, *12*, 2009–2017.

(40) Koç, T.; Marchini, F.; Rousse, G.; Dugas, R.; Tarascon, J.-M. In Search of the Best Solid Electrolyte-Layered Oxide Pairing for Assembling Practical All-Solid-State Batteries. *ACS Appl. Energy Mater.* **2021**, *4*, 13575–13585.

(41) Koç, T.; Hallot, M.; Quemin, E.; Hennequart, B.; Dugas, R.; Abakumov, A. M.; Lethien, C.; Tarascon, J.-M. Toward Optimization of the Chemical/Electrochemical Compatibility of Halide Solid Electrolytes in All-Solid-State Batteries. *ACS Energy Lett.* **2022**, *7*, 2979–2987.

(42) Kim, J. S.; Jung, S.; Kwak, H.; Han, Y.; Kim, S.; Lim, J.; Lee, Y. M.; Jung, Y. S. Synergistic Halide-Sulfide Hybrid Solid Electrolytes for Ni-rich Cathodes Design Guided by Digital Twin for All-Solid-State Li Batteries. *Energy Storage Mater.* **2023**, *55*, 193–204.

(43) Ye, Q.; Li, X.; Zhang, W.; Xia, Y.; He, X.; Huang, H.; Gan, Y.; Xia, X.; Zhang, J. Slurry-Coated $LiNi_{0.8}Co_{0.1}Mn_{0.1}O_2$–$Li_3InCl_6$ Composite Cathode with Enhanced Interfacial Stability for Sulfide-Based All-Solid-State Batteries. *ACS Appl. Mater. Interfaces* **2023**, *15*, 18878–18888.

(44) Lee, D.; Mesnier, A.; Manthiram, A. Crack-Free Single-Crystalline $LiNiO_2$ for High Energy Density All-Solid-State Batteries. *Adv. Energy Mater.* **2024**, 2303490.

(45) Luo, Q.; Liu, C.; Wei, C.; Wu, Z.; Wang, Y.; Li, L.; Jiang, Z.; Ming, L.; Yang, J.; Zhang, L.; others Deep insight of interfacial stability of LiNi0. 7Co0. 1Mn0. 2O2-based all-solid-state battery with superior performances. *Journal of Power Sources* **2024**, *608*, 234616.

(46) Wenzel, S.; Leichtweiss, T.; Krüger, D.; Sann, J.; Janek, J. Interphase formation on lithium solid electrolytes—An in situ approach to study interfacial reactions by photoelectron spectroscopy. *Solid State Ionics* **2015**, *278*, 98–105.

(47) Wang, L.; Maxisch, T.; Ceder, G. Oxidation Energies of Transition Metal Oxides within the GGA+U Framework. *Phys. Rev. B* **2006**, *73*, 195107.

(48) Jain, A.; Hautier, G.; Ong, S. P.; Moore, C. J.; Fischer, C. C.; Persson, K. A.; Ceder, G. Formation Enthalpies by Mixing GGA and GGA+U Calculations. *Phys. Rev. B* **2011**, *84*, 045115.

(49) Kubaschewski, O.; Alcock, C. B. *Metallurgical Thermochemistry*; Pergamon Press, 1979; p 449.

(50) Brown, P. L.; Curti, E.; Grambow, B. *Chemical Thermodynamics of Zirconium*; Elsevier: Amsterdam, 2005; Vol. 8.

(51) Belsky, A.; Hellenbrandt, M.; Karen, V. L.; Luksch, P. New Developments in the In-

organic Crystal Structure Database (ICSD): Accessibility in Support of Materials Research and Design. *Acta Crystallogr., Sect. B: Struct. Sci.* **2002**, *58*, 364–369.

(52) Jain, A.; Ong, S. P.; Hautier, G.; Chen, W.; Richards, W. D.; Dacek, S.; Cholia, S.; Gunter, D.; Skinner, D.; Ceder, G.; Persson, K. A. Commentary: The Materials Project: A Materials Genome Approach to Accelerating Materials Innovation. *APL Mater.* **2013**, *1*, 011002.

(53) Schwietert, T. K.; Arszelewska, V. A.; Wang, C.; Yu, C.; Vasileiadis, A.; De Klerk, N. J. J.; Hageman, J.; Hupfer, T.; Kerkamm, I.; Xu, Y.; Van Der Maas, E.; Kelder, E. M.; Ganapathy, S.; Wagemaker, M. Clarifying the Relationship between Redox Activity and Electrochemical Stability in Solid Electrolytes. *Nat. Mater.* **2020**, *19*, 428–435.

(54) Deiseroth, H.-J.; Kong, S.-T.; Eckert, H.; Vannahme, J.; Reiner, C.; Zaiß, T.; Schlosser, M. Li_6PS_5X: A Class of Crystalline Li-Rich Solids With an Unusually High Li^+ Mobility. *Angew. Chem. Int. Ed.* **2008**, *47*, 755–758.

(55) Boulineau, S.; Courty, M.; Tarascon, J.-M.; Viallet, V. Mechanochemical synthesis of Li-argyrodite Li_6PS_5X (X=Cl, Br, I) as sulfur-based solid electrolytes for all solid state batteries application. *Solid State Ionics* **2012**, *221*, 1–5.

(56) Rao, R. P.; Adams, S. Studies of lithium argyrodite solid electrolytes for all-solid-state batteries. *physica status solidi (a)* **2011**, *208*, 1804–1807.

(57) Stadler, F.; Fietzek, C. Crystalline Halide Substituted Li-Argyrodites as Solid Electrolytes for Lithium Secondary Batteries. *ECS Trans.* **2010**, *25*, 177–183.

(58) Zhu, Y.; He, X.; Mo, Y. First Principles Study on Electrochemical and Chemical Stability of Solid Electrolyte–Electrode Interfaces in All-Solid-State Li-ion Batteries. *J. Mater. Chem. A* **2016**, *4*, 3253–3266.

(59) Pauling, L. *The Nature of the Chemical Bond*; Cornell University Press, 1960.

(60) Wang, S.; Bai, Q.; Nolan, A. M.; Liu, Y.; Gong, S.; Sun, Q.; Mo, Y. Lithium Chlorides and Bromides as Promising Solid-State Chemistries for Fast Ion Conductors with Good Electrochemical Stability. *Angew. Chem. Int. Ed.* **2019**, *58*, 8039–8043.

(61) Blöchl, P. E. Projector Augmented-Wave Method. *Phys. Rev. B* **1994**, *50*, 17953–17979.

(62) Kresse, G.; Furthmüller, J. Efficient Iterative Schemes for *Ab Initio* Total-Energy Calculations Using a Plane-Wave Basis Set. *Phys. Rev. B* **1996**, *54*, 11169–11186.

(63) Perdew, J. P.; Burke, K.; Ernzerhof, M. Generalized Gradient Approximation Made Simple. *Phys. Rev. Lett.* **1996**, *77*, 3865–3868.

(64) Ong, S. P.; Richards, W. D.; Jain, A.; Hautier, G.; Kocher, M.; Cholia, S.; Gunter, D.; Chevrier, V. L.; Persson, K. A.; Ceder, G. Python Materials Genomics (Pymatgen): A Robust, Open-Source Python Library for Materials Analysis. *Comput. Mater. Sci.* **2013**, *68*, 314–319.

(65) Ong, S. P.; Wang, L.; Kang, B.; Ceder, G. Li-Fe-P-O_2 Phase Diagram from First Principles Calculations. *Chem. Mater.* **2008**, *20*, 1798–1807.